SCIENCE CHINA
Technological Sciences

•Article•

July 2024 Vol.67 No.7: 2087–2098
https://doi.org/10.1007/s11431-023-2512-x

Transient Monte Carlo simulation of phonon transport in silicon nanofilms with the local heat source

LI JiaQi[1], CAI JiuQing[2], LI Rui[2*], LIU ZhiChun[1*] & LIU Wei[1]

[1] *School of Energy and Power Engineering, Huazhong University of Science and Technology, Wuhan 430074, China;*
[2] *Wuhan Second Ship Design and Research Institute, Wuhan 430205, China*

Received July 10, 2023; accepted September 19, 2023; published online June 21, 2024

Accurate prediction of junction temperature is crucial for the efficient thermal design of silicon nano-devices. In nano-scale semiconductor devices, significant ballistic effects occur due to the mean free path of phonons comparable to the heat source size and device scale. We employ a three-dimensional non-gray Monte Carlo simulation to investigate the transient heat conduction of silicon nanofilms with both single and multiple heat sources. The accuracy of the present method is first verified in the ballistic and diffusion limits. When a single local heat source is present, the width of the heat source has a significant impact on heat conduction in the domain. Notably, there is a substantial temperature jump at the boundary when the heat source width is 10 nm. With increasing heat source width, the boundary temperature jump weakens. Furthermore, we observe that the temperature excitation rate is independent of the heat source width, while the temperature influence range expands simultaneously with the increase in heat source width. Around 500 ps, the temperature and heat flux distribution in the domain stabilize. In the case of dual heat sources, the hot zone is broader than that of a single heat source, and the temperature of the hot spot decreases as the heat source spacing increases. However, the mean heat flux remains unaffected. Upon reaching a spacing of 200 nm between the heat sources, the peak temperature in the domain remains unchanged once a steady state is reached. These findings hold significant implications for the thermal design of silicon nano-devices with local heat sources.

phonon transport, Monte Carlo simulation, transient heat conduction, silicon nanofilms, local heat source

Citation: Li J Q, Cai J Q, Li R, et al. Transient Monte Carlo simulation of phonon transport in silicon nanofilms with the local heat source. Sci China Tech Sci, 2024, 67: 2087–2098, https://doi.org/10.1007/s11431-023-2512-x

1 Introduction

To obtain more powerful chips, the integration density of electronic components needs to be significantly increased. Integrated circuits (IC) are moving toward more miniaturization with the same chip size. Currently, the size of transistor gates in IC has reached about 10 nm and is working towards the scale of 1 nm [1]. However, the high density and miniaturization of IC lead to remarkably high local heat flux. They cannot be effectively conducted to the top of the chip and exported through the heat sink. The influence of high heat flux is more evident in field effect transistor (FET) devices [2] such as high electron mobility transistor (HEMT) [3] and metal oxide semiconductor field effect transistor (MOSFET) [4]. Therefore, the thermal transport properties in nanostructures are crucial for the thermal management of electronic devices [5,6].

Nowadays, silicon-based semiconductors still dominate the microelectronic device industry. Phonons are the leading hot carriers in nonmagnetic semiconductor crystals such as silicon [7–9]. Compared with metals, the contribution of electrons in semiconductors to heat transport is negligible at room temperature. Under external perturbations, the drift of phonons causes the system to deviate from the thermodynamic equilibrium, which is then restored by phonon-phonon scattering [10]. At the macroscopic scale, the

*Corresponding authors (email: learoylr@163.com; zcliu@hust.edu.cn)

number of phonon-phonon scattering times is enough to fix the thermodynamic equilibrium for diffusion heat transport. The diffusion heat transport is still applicable to Fourier's law. However, in nanostructures, when the size of the research object is equal to the mean free path (MFP) of the carrier, or the time scale of the study is equivalent to the mean scattering time of the carrier, Fourier's law will no longer apply due to the effect of ballistic heat transport [7,8].

The Boltzmann transport equation (BTE) is commonly used to model heat conduction when Fourier's law fails, and it can describe both equilibrium and non-equilibrium phenomena of heat conduction [8,10–13]. When the characteristic length of the system is larger than the wavelength of the phonon, the phonon can be treated as a particle without considering its wave nature. Based on this, phonons can be treated as particles for drift and collisions. BTE is applied from the continuous medium scale to the nano-scale, especially for heat conduction where the model scale is too large for molecular dynamics and first-principles approaches [14,15]. The numerical simulation methods based on BTE generally include two categories: (1) deterministic methods [16–18], such as lattice Boltzmann method (LBM) [19–21] and discrete coordinate method (DOM) [22–24]; (2) stochastic statistical methods, such as Monte Carlo (MC) [25–27]. MC is a method based on repeated random sampling and statistical analysis. A calculated particle represents a collection of many real phonons, and the drift of particles follows the laws of motion of classical mechanics, while a random collision model realizes the interaction between particles. As a stochastic method, MC avoids directly solving the higher-order collision terms of the equations and can describe the motion of particles intuitively [14]. MC is widely used in micro- and nano-scale heat transfer. Mazumder and Majumdar [10] proposed a classical phonon MC simulation scheme to study the thermal conductivity of silicon at different temperatures. The three-phonon scattering was completed by re-sampling from the equilibrium distribution to generate new phonons, considering the non-linear dispersion relationships and dual polarizations of phonons. Lacroix [28] presented a phonon distribution function in the scattering process and applied it to MC simulation. The function reset the phonon for three-phonon scattering and studied the phonon propagation in silicon and germanium. Mittal and Mazumder [29] described and implemented a procedure for calculating three-phonon processes and evaluated the effects of various phonon modes, especially optical phonons, which were neglected in previous MC simulations. The acoustic branch dominates the heat transfer process, but the role of the optical branch in the scattering process is also difficult to ignore. By introducing the equilibrium temperature, Péraud and Hadjiconstantinou [11,12] proposed an energy-based BTE method with variance reduction. Random particles only solve the deviation from the equilibrium distribution. This method can solve any small signal (e.g., temperature difference) at a small constant cost, significantly advancing the progress of MC solving phonon BTE. In recent years, researchers have paid more attention to the effect of internal heat source and self-heating on heat transport in nanostructures [30–34]. Hua and Cao [35] used MC to consider the impact of temperature difference driving versus internal heat source driving on the in-plane effective thermal conductivity of nanofilms. The results show that phonon boundary scattering significantly inhibits the in-plane thermal transport in nanofilms driven by an internal heat source, leading to more extraordinary temperature rise and slower thermal response rate. Nghiem et al. [36] studied the heat conduction near a nano-scale heat source. They used a two-dimensional (2D) discretized simplified model and compared the MC calculations with a Fourier's law-based finite element method (FEM) to study the influence of the heat source width on interface temperature and heat flux. Hua et al. [37] believed predicting junction temperature is crucial in HEMT. The results show a powerful ballistic effect occurs when the phonon MFP is comparable to the hot spot scale, which significantly changes the temperature profile in the channel, and the thermal resistance near the junction increases significantly. In addition, some scholars have studied near-junction heat conduction in power or radio-frequency (RF) devices. Rezgui et al. [38] reported the ultrafast transient heat transport in sub 7-nm Silicon on Insulator (SOI)-FinFETs based on the phonon hydrodynamic equation. They highlight the physical picture of nano-scale heat transport, giving ways to improve the heat management of nano-electronic devices. Chaudhary et al. [39] used 3D technology computer aided design (TCAD) simulators to investigate the self-heating effect (SHE) on the performance of SOI dual material gate (DMG) FinFETs in underlap and overlap configurations for RF/analog applications. Among the three devices under investigation, lower values of thermal parameters for overlap structure make it a suitable candidate for analog/RF applications. Medlar and Hensel [40] applied a statistical phonon transport model (SPTM) to predict nonequilibrium phonon transport in an SOI-FinFET array transistor. Simulation results indicated an excess build-up of up to 17% optical phonons giving rise to transient local temperature hot spots of 37 K in the drain region. However, as far as we know, the transient heat conduction in silicon nanofilms with multiple local heat sources has been less studied by researchers.

2 Method

Firstly, the deviational energy-based BTE used in this paper is briefly introduced. The theoretical details of BTE can be referred to ref. [13]. The semi-classical description of the

evolution of the phase spatial density distribution for dilute phonon gas without external force is as follows:

$$\frac{\partial f}{\partial t}+\nabla_{\mathbf{k}}\,\omega(\mathbf{k},p)\cdot\nabla_{\mathbf{x}}f=\left.\frac{\partial f}{\partial t}\right|_{coll}, \tag{1}$$

where f is the probability distribution function of a single particle, t is the time term, ω is the phonon frequency, which is related to the wave vector $\mathbf{k}$ through the dispersion relation. p represents the phonon polarization and $\left.\frac{\partial f}{\partial t}\right|_{coll}$ is the collision operator. The equilibrium solution of eq. (1) at temperature T is given by Bose-Einstein distribution:

$$f^{eq}(\omega,T)=\frac{1}{\exp\left(\frac{\hbar\omega}{k_BT}\right)-1}. \tag{2}$$

To solve the BTE, a simplified model usually approximates the collision operator. The commonly used method is relaxation time approximation (RTA) [8]. RTA assumes that phonon-phonon scattering makes the system reach local equilibrium f^{loc}. For a constant relaxation time τ, there is

$$\left.\frac{\partial f}{\partial t}\right|_{coll}=-\frac{f-f^{loc}}{\tau}, \tag{3}$$

where τ is usually written as $\tau(\omega,p,T)$ to reflect the complexity of phonon-phonon scattering under different ω, p and T, therefore, under the RTA, eq. (1) can be simplified as

$$\frac{\partial f}{\partial t}+\nabla_{\mathbf{k}}\,\omega(\mathbf{k},p)\cdot\nabla_{\mathbf{x}}f=\frac{f^{loc}-f}{\tau(\omega,p,T)}, \tag{4}$$

where f^{loc} is the Bose-Einstein distribution at pseudo temperature T_{loc}. Here, T_{loc} is calculated by using the equal energy of the phonons consumed and newly generated in the scattering process as

$$\begin{aligned}&\sum_p\int\frac{\hbar\omega f(\mathbf{x},\omega,\theta,\phi,p,t)}{\tau(\omega,p,T)}\frac{D(\omega,p)}{4\pi}\sin\theta\mathrm{d}\omega\mathrm{d}\theta\mathrm{d}\phi\\&=\sum_p\int\frac{\hbar\omega f^{eq}(\omega,T_{loc})}{\tau(\omega,p,T)}D(\omega,p)\mathrm{d}\omega,\end{aligned} \tag{5}$$

where θ and ϕ are polar and azimuthal angle in spherical coordinate respectively, and the density of states $D(\omega,p)$ is calculated as

$$D(\omega,p)=\frac{k^2(\omega,p)}{2\pi V_g(\omega,p)}, \tag{6}$$

where $V_g(\omega,p)\equiv\left\|\nabla_{\mathbf{x}}\omega(\mathbf{k},p)\right\|$ is the phonon group velocity.

The traditional MC solution applied to eq. (4) does not strictly satisfy the energy conservation in the scattering process, and the energy fluctuates around its average value. These fluctuations increase the measured statistical uncertainty and produce deviations by interacting with other fluctuation processes of the system [13]. Recasting BTE in energy form can satisfy energy conservation [11]. By multiplying $\hbar\omega$ by eq. (4) and defining $e=\hbar\omega f$ and $e^{loc}=\hbar\omega f^{loc}$, we obtain the energy-based BTE:

$$\frac{\partial e}{\partial t}+\mathbf{V_g}\cdot\nabla_{\mathbf{x}}e=\frac{e^{loc}-e}{\tau(\omega,p,T)}, \tag{7}$$

where $\mathbf{V_g}=\nabla_{\mathbf{k}}\,\omega(\mathbf{k},p)$ is the phonon group velocity. In the above formula, each calculated particle represents a fixed energy packet e, and strict energy conservation is achieved by fixing the number of particles. In this method, the equilibrium energy distribution $e^{eq}_{T_{eq}}=\hbar\omega f^{eq}\left(\omega,T_{eq}\right)$ is a control variable, and we only focus on the deviation from the equilibrium energy distribution $e^d=e-e^{eq}_{T_{eq}}$. The deviation form of eq. (7) is as follows:

$$\frac{\partial e^d}{\partial t}+\mathbf{V_g}\cdot\nabla_{\mathbf{x}}e^d=\frac{e^{loc}-e^{eq}_{T_{eq}}-e^d}{\tau(\omega,p,T)}, \tag{8}$$

which is assumed that the equilibrium temperature T_{eq} is independent of $\mathbf{x}$ and t. When $\left(T-T_{eq}\right)\ll T_{eq}$, the control variable $e^{eq}_{T_{eq}}$ is close to the actual energy distribution e, the energy deviation is minimal, providing an ideal condition for variance reduction.

Next, the specific implementation process of using MC method to solve BTE is introduced, as shown in Figure 1. We use phonon tracing MC, which simulates phonon trajectories independently, significantly reducing calculation costs compared to direct simulation MC [12,41]. In phonon tracing MC, BTE is solved by time discretization, and each time step is divided into a collision-free advection sub-step and a subsequent scattering sub-step. Before the calculation, the previously calculated phonon states are input. The phonon states used in this paper are quoted from reference [14,42]. There are 20700 phonon frequencies and their corresponding group velocity V_g, relaxation time τ and heat capacity C, as shown in Figure 2. The predicted bulk thermal conductivity is 147.7 W/(m K). Then, the particles (energy packets) are initialized and emitted from the source. It should be pointed out that the total number of particles N should be specified during initialization. Next, the particles drift and determine whether they encounter the boundary. After that, the contribution of the particles to the macroscopic temperature T and heat flux q during the travel is counted. Suppose the volume of the sampled discrete domain is V, in that case, the contribution of the particle to the energy density is $s_i\mathcal{E}^d_{eff}/V$, where s_i is a symbolic parameter given by the positive and negative of e^d, and $\mathcal{E}^d_{eff}$ is effective deviational energy of the particle. The temperature deviation from the equilibrium baseline is $T_{dev}=s_i\mathcal{E}^d_{eff}/CV$, where C is the volume specific heat capacity, and the x direction (or y or z) heat flux is $q_x=s_i\mathcal{E}^d_{eff}V_{g,x}/V$, where $V_{g,x}$ is the x-component of the particle velocity. The ballistic drift of particles is interrupted by

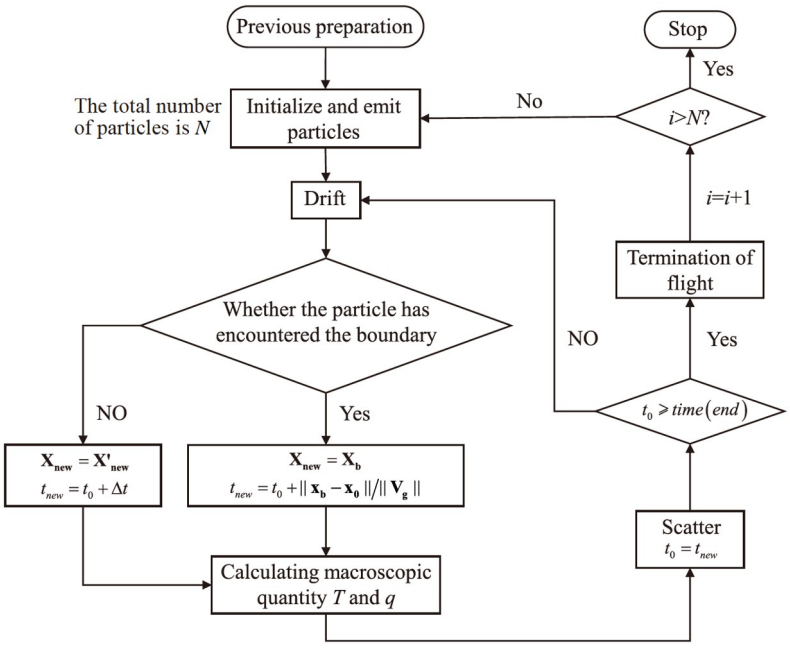

Figure 1 MC simulation procedure.

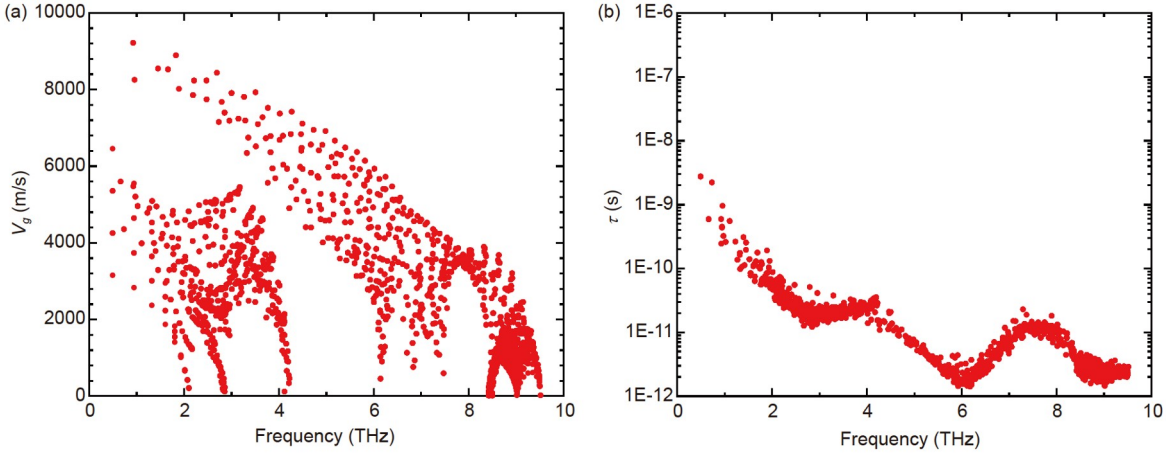

Figure 2 (Color online) Input phonon parameters. (a) Phonon group velocity, V_g; (b) phonon-phonon scattering relaxation time, τ [14].

various phonon scatterings, such as phonon-phonon scattering, boundary scattering, and impurity scattering. Then, whether the particle travel time reaches the preset time is determined. If it does not reach, it continues to drift. Otherwise, the flight is terminated. Finally, N particles are traversed. Our code can obtain the temperature and heat flux values in three directions of each space unit in the simulation domain at each time.

3 Model and method verification

This section introduces the silicon nanofilm model, its boundary conditions, and other computational parameters. After that, the accuracy of the MC algorithm is verified in the ballistic and diffusion limits.

3.1 Model and boundary conditions

This study establishes a silicon nanofilm model, and the schematic diagram is shown in Figure 3. The width of the film is w, and the thickness is t. In the calculation, the number of calculated particles is 10^7, and the simulation domain is discretized into spatial elements uniformly distributed in x, y, and z directions. The top and bottom are the constant temperature boundary conditions, and the in-plane direction (x, y directions) is the periodic boundary conditions. Simulations are carried out on a computer with an Intel(R) Core(TM) i7-

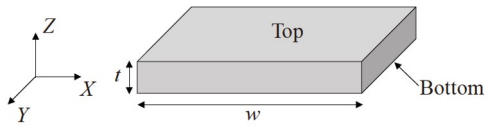

Figure 3 Silicon nanofilm model.

10700 CPU of 2.90 GHz and 16.0 GB RAM.

3.2 Method verification

The ballistic and diffusion limits of our model are verified respectively, to prove the accuracy of the MC algorithm. For the ballistic limit, the equilibrium temperature in the calculation domain is 300 K. Initially, the top's temperature is 310 K, the bottom's temperature is 290 K, and the circumferential boundary is periodic. τ is set to 1 s to ensure that the particle transfer process is ballistic. In the case of ballistic transport, the analytical solution of temperature deviation from equilibrium temperature is given by ref. [11].

$$\Delta T(z,t)=\frac{1}{2}\left(1-\frac{z}{V_g t}\right)H\left(1-\frac{z}{V_g t}\right)\Delta T_h +\frac{1}{2}\left(1-\frac{L-z}{V_g t}\right)H\left(1-\frac{L-z}{V_g t}\right)\Delta T_c, \tag{9}$$

where H is Heaviside function, and L is the length in the z direction. The MC solution of the z direction temperature distribution is compared with the ballistic analytical solution, as shown in Figure 4(a), and the results are in good agreement. At the 100 nm scale, the temperature in the calculation domain has changed at 0.1 ps. We notice that the temperature at the boundary is discontinuous. When t = 10 ps, the temperature in the region near the boundary jumps further. When t = 50 ps, the temperature in the domain reaches the Casimir limit. Then, the calculation domain is reduced, and the temperature difference is expanded to verify the model's accuracy. The calculation domain is 10 nm × 10 nm × 10 nm, and the equilibrium temperature is 325 K. At the initial moment, the top's temperature is 350 K, and the bottom's temperature is 300 K. The rest of the conditions are kept consistent. The MC solution of the z direction temperature distribution is also compared with the analytical solution, as shown in Figure 4(b), and the results are also in good agreement. Due to the computational domain decreasing, it is necessary to monitor the temperature change in the domain for a shorter time after the simulation begins. When t = 0.01 ps, the temperature in the domain starts to change. The same situation as described above occurs when t = 1 ps, with a further temperature jump in the domain near the boundary, reaches the Casimir limit at t = 5 ps.

For the diffusion limit, we compare the MC solution with the 1D Fourier heat conduction equation without an internal heat source in a steady state, which is expressed as

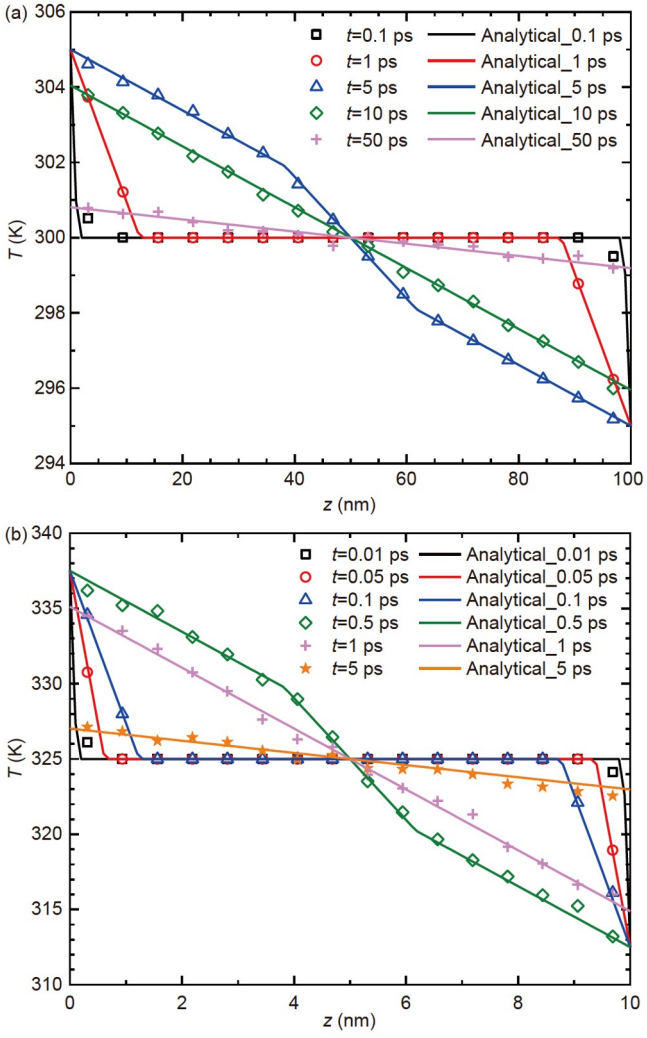

Figure 4 (Color online) Ballistic limit verification, comparison of MC and ballistic analytical solutions. (a) The calculation domain is 100 nm × 100 nm × 100 nm. (b) The calculation domain is 10 nm × 10 nm × 10 nm.

$$\nabla\cdot(k\nabla T)=0. \tag{10}$$

The calculation domain is 5000 nm × 5000 nm × 5000 nm, and the equilibrium temperature is 300 K. The temperature of the top boundary is 310 K, the bottom is 290 K, and the boundary of the x and y direction is periodic. The calculation results are shown in Figure 5. It can be seen that when t = 50 ns, the temperature in the domain solved by the MC method is basically the same as the result of the solution of Fourier's law and then basically no longer changes.

4 Results and discussion

4.1 Transient thermal transport with a single heat source

In this subsection, we study the heat conduction inside the silicon nanofilm in the presence of a single local heat source. The simulated structure is shown in Figure 6. Inspired by the

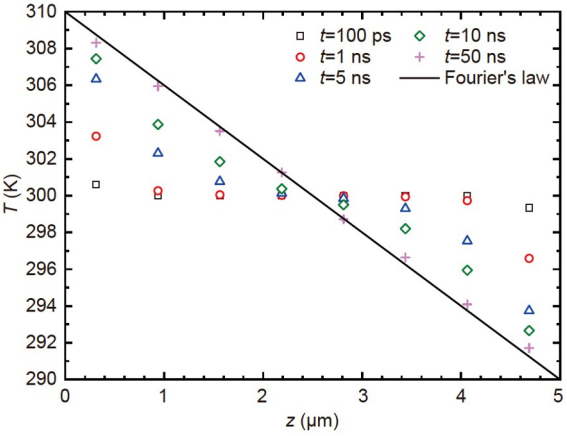

Figure 5 Diffusion limit verification, comparison of MC solution and Fourier's law.

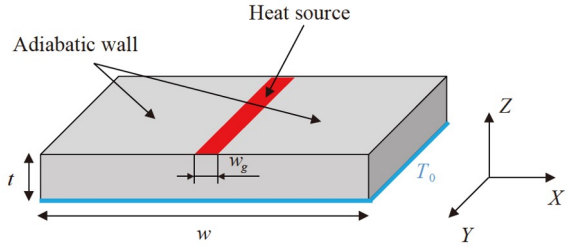

Figure 6 Structure of silicon nanofilm with a single local heat source.

hot spot of the transistor located at the top of the device layer at the gate near the drain [2], the heat source is located in the center of the top of the structure, with a temperature of 380 K. The bottom's temperature is 300 K. In addition to the heat source, the top is an adiabatic boundary and specular reflection, the bottom is a constant temperature boundary, and the in-plane direction is a periodic boundary. We set w = 1000 nm, the length of y direction is the same as x direction, t = 100 nm, heat source width = 10, 20, and 30 nm, that is w_g/w = 0.01, 0.02, and 0.03. The temperature distribution along x direction at y = 500 nm and z = 100 nm in different w_g/w is shown in Figure 7(a)–(c). We define the dimensionless temperature $\theta = \frac{T_{x,y=500,z=100} - T_0}{T_s - T_0}$ as a function of the dimensionless x-axis axial distance x/w, where T_s is the temperature of the heat source, T_0 is the heat sink temperature. It can be seen that the dimensionless temperature of the top boundary gradually increases with time, showing a peak shape. In addition, the larger the width of the heat source, the higher the dimensionless temperature. When $w_g \ll w$, due to a considerable thermal spreading resistance around the heat source area, the heat is difficult to diffuse and accumulates around the heat source to form a local high-temperature hot spot, causing irreversible harm to the device.

Restricted by the phonon group velocity, the excitation of

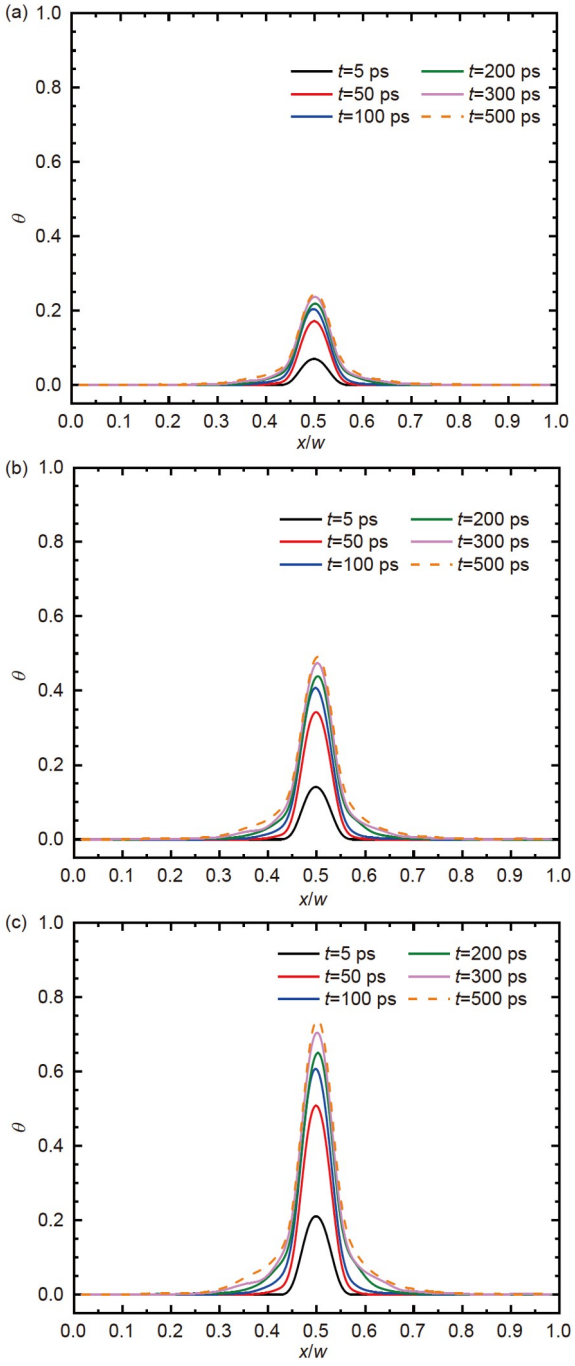

Figure 7 The transient temperature distribution along x direction at y = 500 nm and z = 100 nm with the MC method. (a) w_g/w = 0.01; (b) w_g/w = 0.02; (c) w_g/w = 0.03.

the boundary temperature cannot reach the other side instantaneously but gradually affects the entire film over time. This heat conduction phenomenon is a heat wave [43]. We define the dimensionless temperature $\varphi = \frac{T_{z=50,x=y=500} - T_0}{T_s - T_0}$. As shown in Figure 8, the temperature at z/t = 0.5 changes with time in the films with different w_g/w. At 500 ps, the change of film temperature with time tends to be stable. As

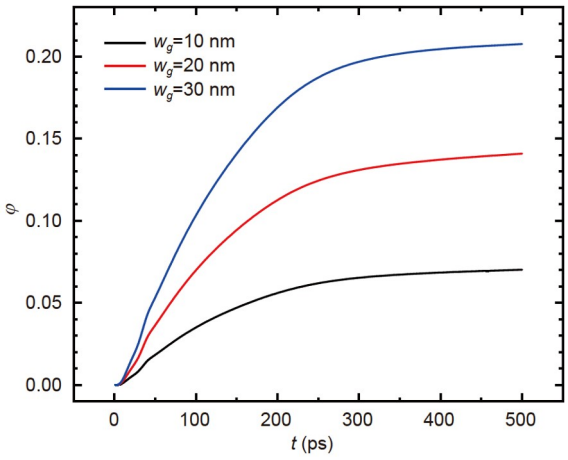

Figure 8 The temperature of a certain position in the film changes with time (z/t = 0.5).

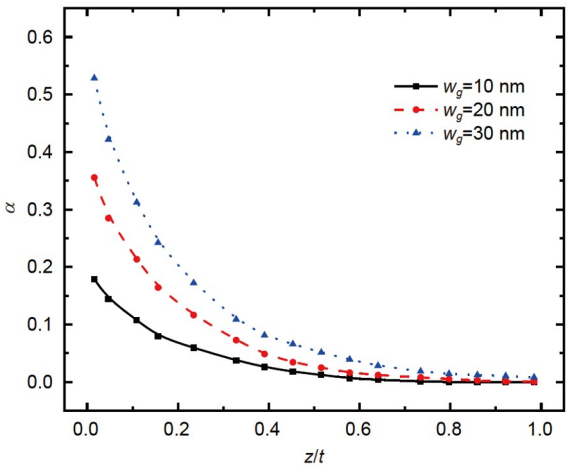

Figure 9 The z direction temperature distribution of nanofilm (t = 50 ps).

the width of the heat source increases, there is no significant difference in the rate of temperature excitation of the film at z/t = 0.5, but the excitation value increases significantly. The temperature excitation rate is known to be mainly related to the Knudsen number and has no direct relationship with the heat source scale.

To further study the heat wave phenomenon, we compared the z direction temperature distribution of silicon nanofilms with different heat source widths at the same time, as shown in Figure 9. We define the dimensionless temperature $\alpha = \frac{T_{z,x=y=500}-T_0}{T_s-T_0}$ as a function of the dimensionless z-axis axial distance z/t. It can be seen that the larger the width of the heat source, the greater the influence range of the heat wave in the film. When the heat source width is 10 nm, the influence of temperature excitation reaches the position of z/t = 0.7. When the heat source width is 20 nm, the influence of temperature excitation reaches the position of z/t = 0.9. When the heat source width is 30 nm, the influence of temperature excitation covers the whole film.

To more accurately determine the time for the system to reach a steady state, we extend the simulation time to 1000 ps. Figure 10 shows the variation of peak temperature with time in the domain. We can observe that as the width of the heat source increases, the temperature rise rate in the domain increases, and the rate of temperature rise gradually slows down over time and finally reaches a steady state at about 500 ps.

For comparison, we use the finite volume method (FVM) to solve the Fourier heat conduction equation to simulate the heat conduction of the system. The temperature distribution of the XZ section at y = 500 nm is shown in Figure 11(a)–(c). There is no boundary temperature jump in diffusion heat transport, and the peak temperature is 380 K. In the case of three heat source widths, the temperature distribution in the domain basically ceases to change at 50 ps; after that, the

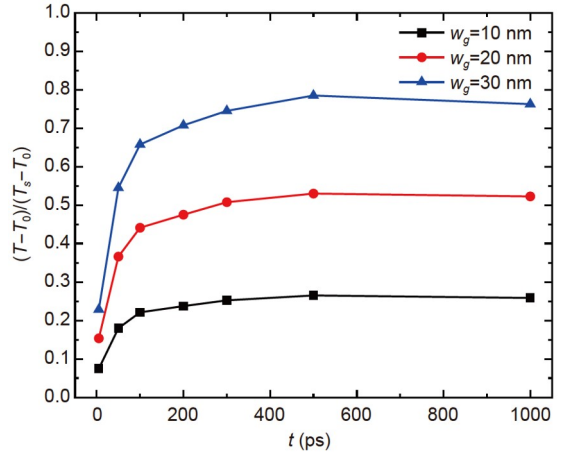

Figure 10 The transient peak temperature in the domain.

average temperature in the domain increases slightly (less than 0.1 K) and reaches a steady state at 150 ps. The system takes much less time to get a steady state under the MC method considering ballistic heat transport. As the width of the heat source increases, the size of the final formed thermal region also gradually increases.

To show the temperature variation in the film thickness direction more visually, we take the temperature values at each point in the z-axis direction at $x = y$ = 500 nm at 500 ps, as shown in Figure 12. MC simulation shows that the temperature decreases more sharply in the early stage away from the heat source direction and then gradually tends to be gentle. However, the Fourier model shows a linear change in the later period. For the same heat source width, the predicted temperature values of the Fourier model are higher than those of the MC model except for the domain near the bottom. In addition, the Fourier model shows a continuous temperature distribution, while the MC model indicates temperature jumps at the top and bottom boundaries. When

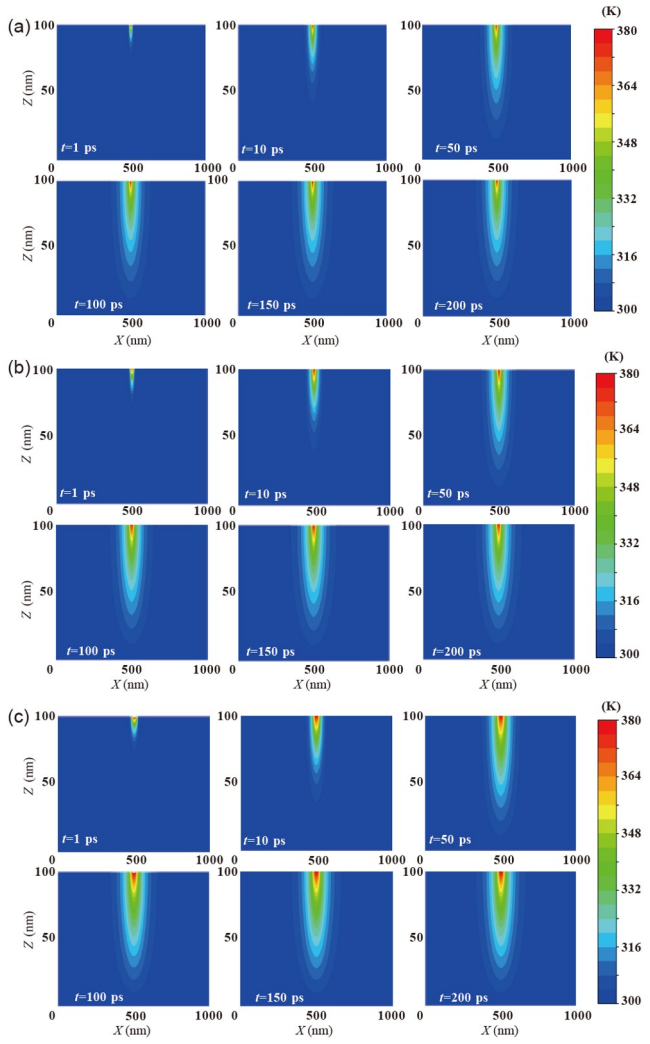

Figure 11 The transient temperature distribution of the *XZ* plane at y = 500 nm with FVM. (a) w_g/w = 0.01; (b) w_g/w = 0.02; (c) w_g/w = 0.03.

$w_g \ll w$, the boundary temperature jump decreases rapidly with the increase of the heat source width. Specifically, the temperature jump is due to the non-equilibrium heat conduction and ballistic properties of phonon transport near the boundary and the definition of local temperature by BTE [7]. In the near-heat source region, when the heat source width is much smaller than the MFP of the phonons, the volume scattering within the system is essentially non-existent. Furthermore, the temperature calculated by MC simulations indicates the mean deviational energy at that position. The larger the temperature jump, the stronger the thermal non-equilibrium near the interface.

In addition, we studied the heat flux in the z direction (q_z) and thermal resistance shown in Table 1. To characterize the thermal spreading resistance, we define the dimensionless total thermal resistance:

$$\frac{R}{R_{1D\_0}} = 1 + \frac{R_{sp}}{R_{1D\_0}}, \tag{11}$$

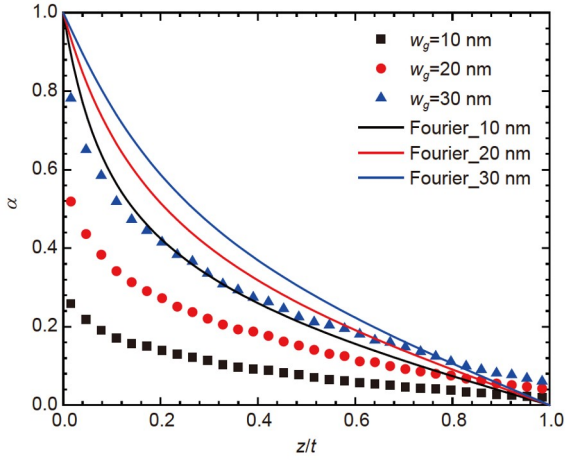

Figure 12 The dimensionless temperature distribution along the z-axis with different heat source widths. The symbol is the MC model, and the solid line is Fourier model.

Table 1 The heat flux and dimensionless total thermal resistance with different heat source widths w_g

w_g (nm)	Maximum heat flux (W/m^2)	$\frac{R}{R_{1D\_0}}$
10	7.51×10^9	42.12
20	1.513×10^{10}	21.28
30	2.235×10^{10}	14.01

where R_{1D_0} is the 1D thermal resistance defined using the intrinsic thermal conductivity k_0, that is, $R_{1D\_0} = t/(wk_0)$. R_{sp} is the thermal spreading resistance. It is known that the evaluation of the dimensionless total thermal resistance is equivalent to the dimensionless thermal spreading resistance. When w_g= 10 nm, the maximum heat flux along x direction reaches 7.51×10^9 W/m^2 when t = 500 ps. When w_g= 20 nm, the maximum reaches 1.513×10^{10} W/m^2, and it reaches 2.235×10^{10} W/m^2 when w_g= 30 nm. It can be seen that with the increase of heat source width, the heat flux increases gradually, which is consistent with the trend of temperature rise. We also calculated the dimensionless total thermal resistance, which decreases with increasing w_g, indicating that the same trend exists for the thermal spreading resistance. That is, the smaller the width of the heat source, the greater the thermal resistance during conduction.

4.2 Transient thermal transport with dual heat sources

This subsection studies heat conduction in silicon nanofilms with dual heat sources. The heat source distribution is shown in Figure 13. Both heat sources have a width of 10 nm and are symmetrically distributed along the x direction of the film. The spacing s between the centers of the heat sources is studied for four cases of 50, 70, 100, and 150 nm. We set w =

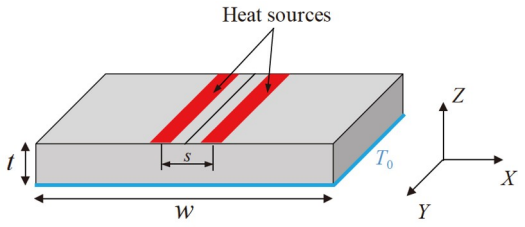

Figure 13 Structure of silicon nanofilm with dual local heat sources.

1000 nm, t = 100 nm, and the boundary conditions are the same as in the previous section. The temperature profile is drawn on the XZ plane when y = 500 nm, as shown in Figure 14(a)–(d). When the spacing s = 50 nm, the hot zone is still whole, and the dual heat sources have no significant effect on the temperature distribution compared with the single heat source, as shown in Figure 14(a). However, the hot zone is more expansive. The peak temperature in the region is 336.9 K, which is 98.4% of the peak temperature of the single heat source with a width of 20 nm. As shown in Figure 14(b), when s = 70 nm, the heat zone appears blocking at the beginning. At 200 ps, a separated high-temperature hot zone appears and expands further. The peak temperature in the domain is 330.6 K, reaching 96.6% of the single heat source with a width of 20 nm. When s = 100 nm, the hot zone in the domain appears to be an apparent block phenomenon. The influence of double heat sources on the temperature distribution is the same, as shown in Figure 14(c). The peak temperature in the domain is 334.8 K, reaching 97.8% of the single heat source with a width of 20 nm. As shown in Figure 14(d), when s = 150 nm, the hot zone generated by the two heat sources is always in a state of separation. The peak temperature in the domain reaches 333.3 K, which is 97.3% of the single heat source with a width of 20 nm. It can be seen that the peak temperature in the domain with different spacing of heat source is smaller than that of the single heat source with the same heat source area. Because with the same heat source area, the larger the number of heat sources, the smaller the single heat source scale, and the stronger the ballistic effect of phonon heat transport, resulting in a more intense boundary temperature jump. In addition, with the increase of the spacing, the range of the hot zone is more expansive, which is easy to understand.

However, the change rule of peak temperature at steady state is still unclear with the increase of heat source spacing. Therefore, we calculated the peak temperature at 500 ps in the domain with of s = 10, 30, 90, 110, 120, 140, 170, 200, 250, and 300 nm for further study are shown in Figure 15. It can be seen that except for the data points with spacing of around 100 and 150 nm, the peak value in the domain decreases rapidly with the increase of spacing. This is because when w_g is comparable with the MFP of the phonons, with the increase of heat source spacing, an equivalent heat source can be formed between the heat sources, equal to increasing the width of the heat source. As the width of the heat source increases, the thermal spreading resistance decreases,

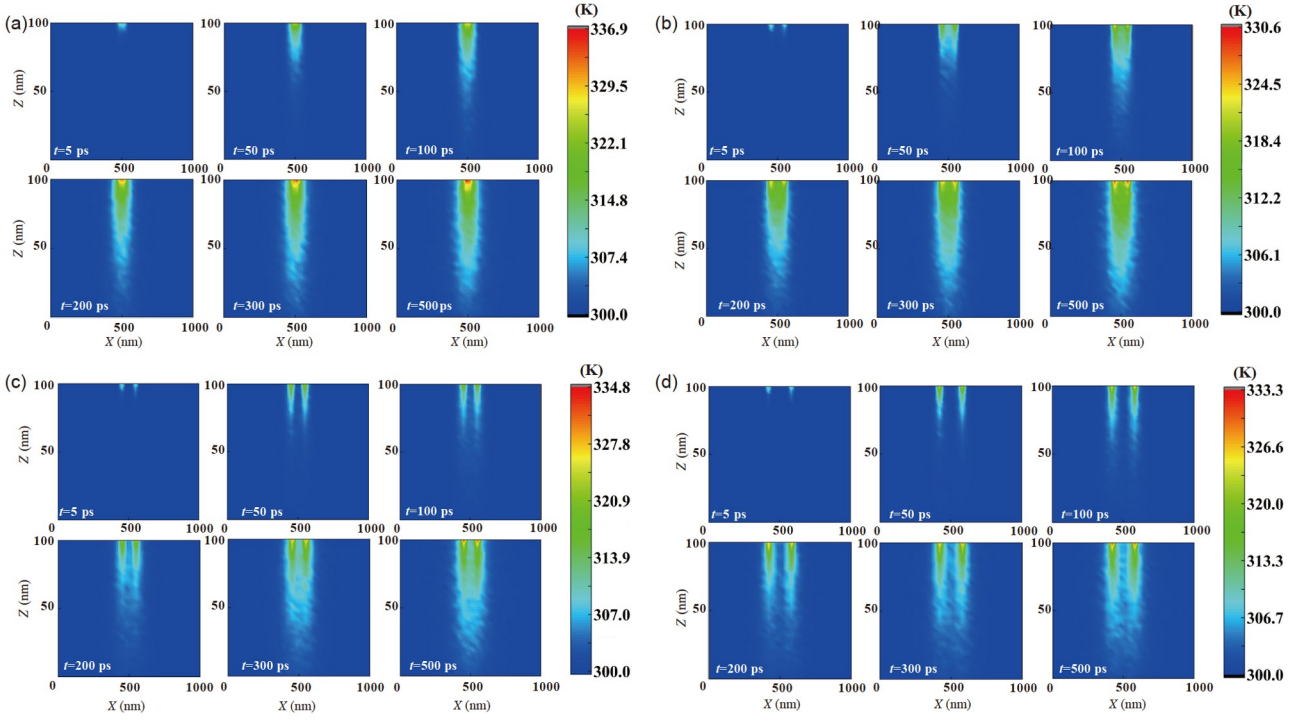

Figure 14 Transient temperature profile in the XZ plane when y = 500 nm with different spacing between dual heat sources. (a) s = 50, (b) 70, (c) 100, and (d) 150 nm.

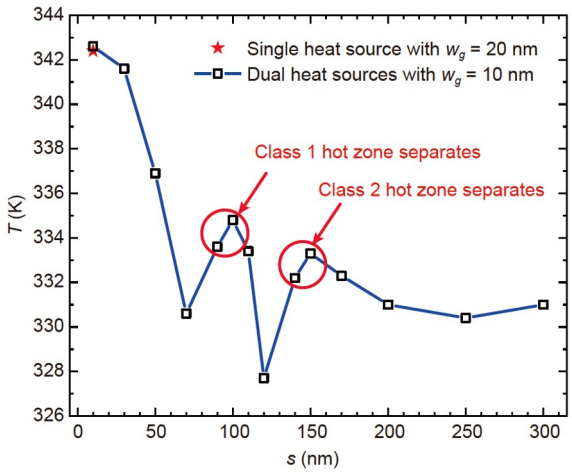

Figure 15 Peak temperature variations in domain with different spacing.

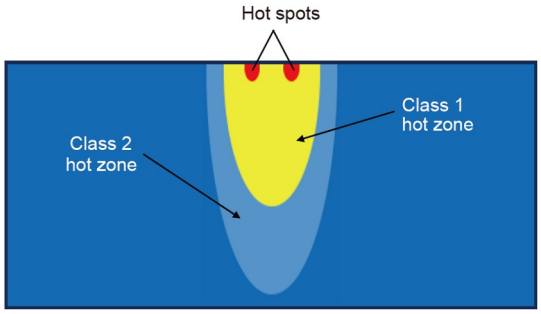

Figure 16 The schematic diagram of the classification of hot zones.

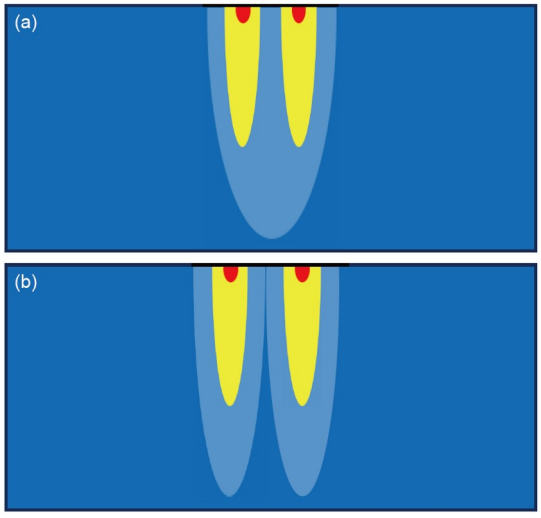

Figure 17 The schematic diagrams of the separation of hot zones. (a) The separation of Class 1 hot zone. (b) The separation of Class 2 hot zone.

allowing the heat at the hot spot to diffuse more quickly, reducing the peak temperature in the domain. When the heat source spacing is 10 nm, the peak temperature is 342.6 K, which is very close to the peak temperature of a single heat source with a heat source width of 20 nm (342.4 K). The idea of limit in mathematics can understand it; that is to say, a single heat source with a width of 20 nm can be regarded as a double heat source with a width of 10 nm which s is 10 nm. When the spacing is greater than 200 nm, the temperature does not change basically, which is about 331 K. To explain the phenomenon of abnormal data points around 100 and 150 nm, we define different classes of hot zones, Class 1 hot zone and Class 2 hot zone, as shown in Figure 16. The schematic diagrams of hot zones separation are shown in Figure 17. From Figure 14, when s is 100 nm, the separation of Class 1 hot zone occurs. The Class 2 hot zone also separates when s is 150 nm. Observed by further calculations, the separation of Class 1 hot zone has appeared initially when the spacing is 90 nm. Similarly, at a spacing of 140 nm, the Class 2 hot zone has started to separate. In addition, there is a trough between the two irregular peak regions; that is when s is 120 nm, the peak temperature in the region is 327.7 K, which is lower than the steady-state value after the spacing is 200 nm. The phenomenon of different classes of hot zone separation at a specific spacing is the cause of irregular local data points. The separation of hot zones at different classes represents essential nodes in the gradual weakening of the joint influence of the dual heat sources with increased heat source spacing, and irregular data points appear near these nodes. This reflects the complexity of micro-nano scale heat conduction in the case of multiple heat sources. The finding is significant for the thermal design of multi-heat sources silicon nano-devices.

We also analyze the heat flux distribution with the influence of double heat sources, as shown in Figure 18. When s = 50 nm, the influence of double heat sources on the heat flux has not yet appeared, and its distribution is still in the form of a single peak. The maximum heat flux reaches 1.290×10^{10} W/m^2 when t = 500 ps. When s = 100 nm, the q_z is double peak type, and the maximum is 1.131×10^{10} W/m^2 when t = 500 ps. When s = 150 nm, the spacing of the two peaks is more extensive, and the maximum value reaches 1.084×10^{10} W/m^2 when t = 500 ps, as shown in Table 2. With the increase of heat source spacing, the variation trend of the maximum heat flux is consistent with that of the peak temperature in the domain, which confirms the accuracy of the hot zone classification theory. We found that the mean heat flux with different heat source spacing is the same, indicating that the difference in heat source spacing will not affect the mean heat flux but only the heat flux distribution under the same heat source width.

5 Conclusions

This study used MC simulation to study the transient thermal transport of phonons in silicon nanofilms with local heat

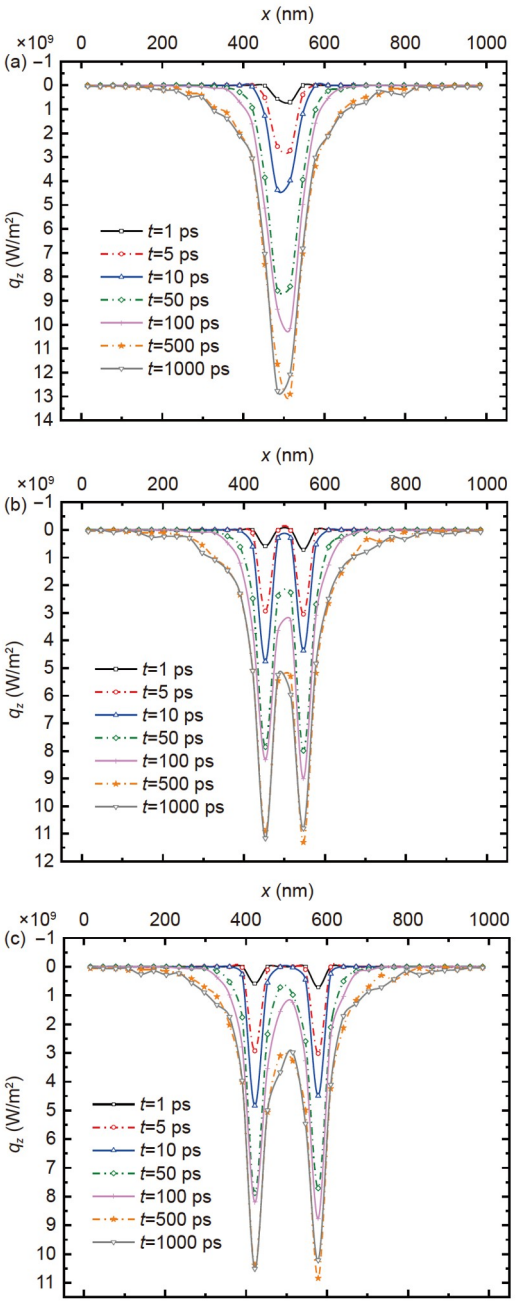

Figure 18 (Color online) The distribution of heat flux in the z direction (q_z) along the x direction. (a) s = 50 nm; (b) 100 nm; (c) 150 nm.

sources. A comparative study was conducted for single and multi-heat source cases. The accuracy of the numerical method is verified by comparing it with the empirical formula in the ballistic limit and Fourier's law in the diffusion limit. The conclusions of this paper are as follows.

(1) In the case of a single heat source, the width of the heat source has a significant influence on the temperature distribution in the domain. The temperature distribution is basically unchanged after 300 ps and reaches a steady state at 500 ps. Due to the non-equilibrium and ballistic properties of phonon transport, there are different degrees of temperature jumps at the top and bottom boundaries of the system. As the heat source width increases, the temperature jump decreases rapidly. However, the width of the heat source has little effect on the temperature excitation rate, and the time when the temperature disturbance is felt at z/t = 0.5 under different heat source widths is basically the same.

Table 2 The heat flux with different heat source spacing s

s (nm)	Maximum heat flux (W/m^2)	Mean heat flux (×10^9 W/m^2)
50	1.290×10^{10}	1.76
70	9.90×10^{9}	1.76
100	1.131×10^{10}	1.76
120	9.67×10^{9}	1.76
150	1.084×10^{10}	1.76

(2) When there are dual heat sources, the peak temperature in the domain when it reaches a steady state is always smaller than that in a single heat source under the same heat source area. This is due to the same heat source area; the more heat sources, the smaller the heat source scale, resulting in a stronger boundary temperature jump. When s = 10 nm, the peak temperature in the domain is essentially identical to the single heat source with a width of 20 nm.

(3) With the increase of the spacing between dual heat sources, the peak temperature in the domain generally shows a downward trend, and it does not change when s = 200 nm. To explain the local irregular phenomenon in the process of spacing change, we put forward the concept of heat zone classification, which is in good agreement with the spacing corresponding to the anomaly point. For the anomaly points around s = 100 nm, the Class 1 hot zone is separated, and for the anomaly points around s = 150 nm, the Class 2 hot zone is divided. In addition, the time points of hot zone separation are also different. When the s = 50 nm, the hot zone will not separate. When the s = 70 nm, the hot zone separates at 5 ps and merges again at 50 ps. As the spacing continues to expand, when the s reaches 100 nm, the Class 1 hot zone remains separated, and the Class 2 hot zone merges again at 300 ps after separation at 5 ps. When the s = 150 nm, the Class 1 and Class 2 hot zones are always separated.

(4) In the case of a single heat source, the maximum and mean values of q_z increase with the increase of heat source width. For dual heat sources, the variation trend of the maximum value of q_z with the heat source spacing is consistent with the peak temperature in the domain, and the mean heat flux remains unchanged. When the temperature difference is constant, the dimensionless total thermal resistance of the nanofilm under the influence of the local heat source is only related to the heat source scale and irrelevant to the spacing between the heat sources.

This work was supported by the National Natural Science Foundation of China (Grant No. 52076088) and the Core Technology Research Project of Shunde District, Foshan, China (Grant No. 2130218002932).

1 Desai S B, Madhvapathy S R, Sachid A B, et al. MoS_2 transistors with 1-nanometer gate lengths. Science, 2016, 354: 99–102
2 Pop E, Sinha S, Goodson K E. Heat generation and transport in nanometer-scale transistors. Proc IEEE, 2006, 94: 1587–1601
3 Chatterjee B, Dundar C, Beechem T E, et al. Nanoscale electro-thermal interactions in AlGaN/GaN high electron mobility transistors. J Appl Phys, 2020, 127: 044502
4 Ni C, Aksamija Z, Murthy J Y, et al. Coupled electro-thermal simulation of MOSFETs. J Comput Electron, 2012, 11: 93–105
5 Chen G, Hu B, Jiang Z, et al. Reconstruction of interfacial thermal transport mediated by hotspot in silicon-based nano-transistors. Int J Heat Mass Transfer, 2023, 202: 123676
6 Moore A L, Shi L. Emerging challenges and materials for thermal management of electronics. Mater Today, 2014, 17: 163–174
7 Cahill D G, Braun P V, Chen G, et al. Nanoscale thermal transport. II. 2003–2012. Appl Phys Rev, 2014, 1: 011305
8 Chen G. Nano-scale Energy Transport and Conversion: A Parallel Treatment of Electrons, Molecules, Phonons, and Photons. Oxford: Oxford University Press, 2005
9 Ziman J M. Electrons and Phonons: The Theory of Transport Phenomena in Solids. Oxford: Oxford University Press, 2001
10 Mazumder S, Majumdar A. Monte Carlo study of phonon transport in solid thin films including dispersion and polarization. J Heat Transfer, 2001, 123: 749–759
11 Péraud J P M, Hadjiconstantinou N G. Efficient simulation of multidimensional phonon transport using energy-based variance-reduced Monte Carlo formulations. Phys Rev B, 2011, 84: 205331
12 Péraud J P M, Hadjiconstantinou N G. An alternative approach to efficient simulation of micro/nanoscale phonon transport. Appl Phys Lett, 2012, 101: 153114
13 Peraud J P M, Landon C D, Hadjiconstantinou N G. Monte Carlo methods for solving the Boltzmann transport equation. Annu Rev Heat Transfer, 2014, 17: 205–265
14 Pathak A, Pawnday A, Roy A P, et al. MCBTE: A variance-reduced Monte Carlo solution of the linearized Boltzmann transport equation for phonons. Comput Phys Commun, 2021, 265: 108003
15 Chen G, Lin X, Liu Y, et al. Monolayer MoS_2-based transistors with low contact resistance by inserting ultrathin Al_2O_3 interfacial layer. Sci China Tech Sci, 2023, 66: 1831–1840
16 Narumanchi S V J, Murthy J Y, Amon C H. Submicron heat transport model in silicon accounting for phonon dispersion and polarization. J Heat Transfer, 2005, 126: 946–955
17 Majumdar A. Microscale heat conduction in dielectric thin films. J Heat Transfer, 1993, 115: 7–16
18 Mao Y D, Xu M T. Non-Fourier heat conduction in a thin gold film heated by an ultra-fast-laser. Sci China Tech Sci, 2015, 58: 638–649
19 Wang D, Qu Z, Ma Y. An enhanced Gray model for nondiffusive heat conduction solved by implicit lattice Boltzmann method. Int J Heat Mass Transfer, 2016, 94: 411–418
20 Chattopadhyay A, Pattamatta A. Energy transport across submicron porous structures: A lattice Boltzmann study. Int J Heat Mass Transfer, 2014, 72: 479–488
21 Chattopadhyay A, Pattamatta A. A comparative study of submicron phonon transport using the Boltzmann transport equation and the lattice Boltzmann method. Numer Heat Transfer Part B-Fundamentals, 2014, 66: 360–379
22 Donmezer F N, Singh D, James W, et al. Lattice Boltzmann and discrete ordinates methods for phonon transport modeling: A comparative study. In: Proceedings of ASME 2011 International Mechanical Engineering Congress and Exposition, Denver: ASME, 2011. 333–343
23 Zhang C, Chen S, Guo Z, et al. A fast synthetic iterative scheme for the stationary phonon Boltzmann transport equation. Int J Heat Mass Transfer, 2021, 174: 121308
24 Zhang C, Guo Z, Chen S. An implicit kinetic scheme for multiscale heat transfer problem accounting for phonon dispersion and polarization. Int J Heat Mass Transfer, 2019, 130: 1366–1376
25 Shen Y, Yang H A, Cao B Y. Near-junction phonon thermal spreading in GaN HEMTs: A comparative study of simulation techniques by full-band phonon Monte Carlo method. Int J Heat Mass Transfer, 2023, 211: 124284
26 Shen Y, Hua Y C, Li H L, et al. Spectral thermal spreading resistance of wide-bandgap semiconductors in ballistic-diffusive regime. IEEE Trans Electron Devices, 2022, 69: 3047–3054
27 Hua Y C, Li H L, Cao B Y. Thermal spreading resistance in ballistic-diffusive regime for GaN HEMTs. IEEE Trans Electron Devices, 2019, 66: 3296–3301
28 Peterson R B. Direct simulation of phonon-mediated heat transfer in a debye crystal. J Heat Transfer, 1994, 116: 815–822
29 Mittal A, Mazumder S. Monte Carlo study of phonon heat conduction in silicon thin films including contributions of optical phonons. J Heat Transfer, 2010, 132: 052402
30 Wong B T, Francoeur M, Pinar Mengüç M. A Monte Carlo simulation for phonon transport within silicon structures at nanoscales with heat generation. Int J Heat Mass Transfer, 2011, 54: 1825–1838
31 Hua Y C, Cao B Y. Transient in-plane thermal transport in nanofilms with internal heating. Proc R Soc A, 2016, 472: 20150811
32 Shen Y, Chen X S, Hua Y C, et al. Bias dependence of non-Fourier heat spreading in GaN HEMTS. IEEE Trans Electron Devices, 2023, 70: 409–417
33 Li H L, Shen Y, Hua Y C, et al. Hybrid Monte Carlo-diffusion studies of modeling self-heating in ballistic-diffusive regime for gallium nitride HEMTs. J Electron Packaging, 2023, 145: 011203
34 Huang J, He Y R, Hui S Y, et al. A review of membrane distillation enhancement via thermal management and molecular transport through nanomaterial-based membranes. Sci China Tech Sci, 2023, 66: 1662–1682
35 Hua Y C, Cao B Y. The effective thermal conductivity of ballistic–diffusive heat conduction in nanostructures with internal heat source. Int J Heat Mass Transfer, 2016, 92: 995–1003
36 Nghiem T T, Trannoy N, Randrianalisoa J. Monte Carlo prediction of ballistic effect on phonon transport in silicon in the presence of small localized heat source. Nanotechnology, 2019, 30: 415403
37 Cheng Y, Ma J, Xu Y, et al. Evolution of in-plane heat transport in tellurium from 2D to 3D. Mater Today Phys, 2022, 27: 100776
38 Rezgui H, Nasri F, Ali A B H, et al. Analysis of the ultrafast transient heat transport in sub 7-nm SOI FinFET technology nodes using phonon hydrodynamic equation. IEEE Trans Electron Devices, 2021, 68: 10–16
39 Chaudhary R, Saha R. Impact of self-heating on RF/analog and linearity parameters of DMG FinFETs in underlap and overlap configurations. MicroElectron J, 2023, 135: 105765
40 Medlar M P, Hensel E C. Transient three-dimensional thermal simulation of a fin field-effect transistor with electron–phonon heat generation, three phonon scattering, and drift with periodic switching. ASME J Heat Mass Transfer, 2023, 145: 022501
41 Li H L, Hua Y C, Cao B Y. A hybrid phonon Monte Carlo-diffusion method for ballistic-diffusive heat conduction in nano- and microstructures. Int J Heat Mass Transfer, 2018, 127: 1014–1022
42 Carrete J, Vermeersch B, Katre A, et al. almaBTE : A solver of the space–time dependent Boltzmann transport equation for phonons in structured materials. Comput Phys Commun, 2017, 220: 351–362
43 Joshi A A, Majumdar A. Transient ballistic and diffusive phonon heat transport in thin films. J Appl Phys, 1993, 74: 31–39